Electric-field-controlled water and ion permeation of a hydrophobic nanopore

J. Dzubiella and J.-P. Hansen

Articles you may be interested in

Ion condensation behavior and dynamics of water molecules surrounding the sodium poly(methacrylic acid) chain in water: A molecular dynamics study
J. Chem. Phys. **136**, 124903 (2012); 10.1063/1.3697477

Comment on "Ab initio molecular dynamics calculation of ion hydration free energies" [J. Chem. Phys.130, 204507 (2009)]
J. Chem. Phys. **133**, 047103 (2010); 10.1063/1.3456164

Comment on "Free energy of solvation of simple ions: Molecular dynamics study of solvation of Cl − and Na + in the ice/water interface" [J. Chem. Phys.123, 034706 (2005)]
J. Chem. Phys. **126**, 237101 (2007); 10.1063/1.2737662

Modeling the selective partitioning of cations into negatively charged nanopores in water
J. Chem. Phys. **126**, 084706 (2007); 10.1063/1.2464083

Free energy of solvation of simple ions: Molecular-dynamics study of solvation of Cl − and Na + in the ice/water interface
J. Chem. Phys. **123**, 034706 (2005); 10.1063/1.1953578

Electric-field-controlled water and ion permeation of a hydrophobic nanopore

J. Dzubiella[a)] and J.-P. Hansen
University Chemical Laboratory, Lensfield Road, Cambridge CB2 1EW, United Kingdom

The permeation of hydrophobic, cylindrical nanopores by water molecules and ions is investigated under equilibrium and out-of-equilibrium conditions by extensive molecular-dynamics simulations. Neglecting the chemical structure of the confining pore surface, we focus on the effects of pore radius and electric field on permeation. The simulations confirm the intermittent filling of the pore by water, reported earlier under equilibrium conditions for pore radii larger than a critical radius R_c. Below this radius, water can still permeate the pore under the action of a strong electric field generated by an ion concentration imbalance at both ends of the pore embedded in a structureless membrane. The water driven into the channel undergoes considerable electrostriction characterized by a mean density up to twice the bulk density and by a dramatic drop in dielectric permittivity which can be traced back to a considerable distortion of the hydrogen-bond network inside the pore. The free-energy barrier to ion permeation is estimated by a variant of umbrella sampling for Na^+, K^+, Ca^{2+}, and Cl^- ions, and correlates well with known solvation free energies in bulk water. Starting from an initial imbalance in ion concentration, equilibrium is gradually restored by successive ion passages through the water-filled pore. At each passage the electric field across the pore drops, reducing the initial electrostriction, until the pore, of radius less than R_c, closes to water and hence to ion transport, thus providing a possible mechanism for voltage-dependent gating of hydrophobic pores. © *2005 American Institute of Physics.* [DOI: 10.1063/1.1927514]

I. INTRODUCTION

The structure and dynamics of water and aqueous solutions near interfaces, or confined to narrow pores differ considerably from bulk behavior under comparable thermodynamic conditions. A well-known example is the high degree of supercooling which can be achieved when water is confined to nanoporous silica materials, allowing the exploration of slow relaxations by a number of experimental and numerical techniques.[1] Furthermore, water molecules are frequently subjected to very large electric fields at interfaces (e.g., near metallic electrodes or highly charged colloids and macromolecules), leading to orientational ordering of the molecules, dielectric saturation,[2] and electrostriction.[3] The joint effect of confinement and strong electric fields is of particular relevance to biological pores, such as aquaporins and ion channels through membranes.[4] In this paper we address the problem of ion and water permeation of model hydrophobic pores, under the action of strong electric fields generated by ion concentration gradients. We restrict our attention to highly simplified models in the hope to gain some generic physical insight. The nanopores will be assumed to be cylinders with smooth surfaces connecting two reservoirs with aqueous solutions. Under equilibrium conditions, in the absence of ions, this simple model has been shown to share with more realistic models of carbon nanotubes[5] or of hydro-

phobic ion channels[6–9] the phenomenon of intermittent filling by water or "liquid/vapor oscillations" of the confined water over a narrow range of pore diameters.[10] This intermittent behavior may provide a gating mechanism for hydrophobic ion channels, whereby the channel is open or closed to ion transport when it is filled or empty of water,[8] a scenario for which some recent experimental evidence has become available.[11]

Coulombic effects on the behavior of water and ions in nanopores are essentially twofold. First, if the pore surface is lined with polar residues, the pore becomes hydrophilic, so that water permeation is enhanced and occurs at smaller pore radii.[8,12] On the other hand, an externally applied electric field along the pore axis will induce water and ion transport. The resulting current–voltage relation can be estimated by continuum theories, such as the Poisson–Nernst–Planck (PNP) formulation of electrodiffusion,[13] kinetic theory,[14] Brownian dynamics (BD),[15] or molecular-dynamics (MD) simulations.[16] The latter work may be considered as simulating a stationary nonequilibrium situation, where ions and water are driven through a channel by a constant uniform applied electric field under periodic boundary conditions, which mimic a closed-circuit situation.[15] These authors observed 12 cation passages over a 100-ns time span, which allowed a statistically reasonable estimate of channel conductance, in semiquantitative agreement with experimental data.

In this paper we go one step further, by considering the permeation of a hydrophobic cylindrical nanopore by water and ions, under the action of the strong electric field gener-

---

[a)]Present address: NSF Center for Theoretical Biological Physics (CTBP), Department of Chemistry and Biochemistry, University of California, San Diego, La Jolla, California 92093-0365. Electronic mail: jdzubiella@ucsd.edu
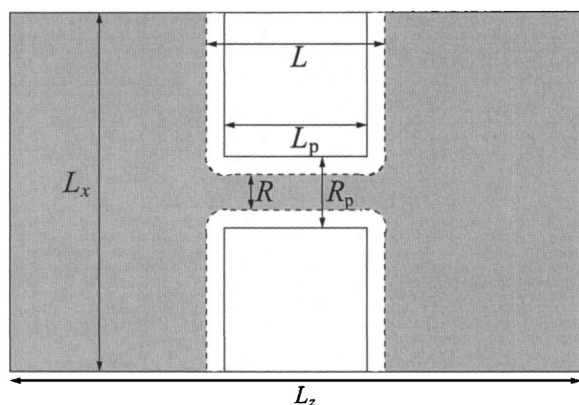
122, 234706-1

FIG. 1. Two-dimensional sketch of the cylindrical model pore with radius R_p and length L_p in a slab of width L_p connecting two reservoirs filled with SPC/E water. The membrane-water interaction reduces the volume accessible to water and defines the effective pore radius R and the effective pore length L. The effective volume inaccessible to water is depicted (white area) by a dashed line. $L_x = L_y$ and L_z are the simulation box lengths.

TABLE I. Summary of the interaction parameters used in this work. The parameters for the cross interactions not given here are obtained by the usual combining rules.

	Interaction	(ϵ/kJ mol^{-1})	(σ/Å)
(a)	O–O	0.6502	3.169
	O–Na$^+$	0.5216	2.876
	O–K$^+$	0.5216	3.250
	O–Ca^{2+}	0.5216	3.019
	O–Cl$^-$	0.5216	3.250
	Na$^+$–Na$^+$	0.3576	2.730
	K$^+$–K$^+$	0.4184	3.331
	Ca^{2+}–Ca^{2+}	0.4184	2.869
	Cl$^-$–Cl$^-$	0.1679	4.860
	Interaction	**(ϵ'/kJ mol^{-1})**	**(σ'/Å)**
(b)	Wall–O	1.2578	2.474
	Wall–Na$^+$	0.9328	2.255
	Wall–K$^+$	0.6393	2.551
	Wall–Ca^{2+}	1.0090	2.324
	Wall–Cl$^-$	1.0090	3.320

ated by a cation concentration gradient across the embedding membrane, and the relaxation of the initial far-from-equilibrium state to a final closed state of the pore of radius R_p less than the threshold radius for water permeation under equilibrium conditions.[10] The scenario observed in the non-equilibrium MD simulations may be a simple example of voltage gating. A preliminary report of parts of the present work was published elsewhere.[17]

II. MODEL AND METHODOLOGY

Consider a cylindrical pore of radius R_p and length L_p, connecting two reservoirs on both sides of an impermeable, nonpolarizable membrane, as sketched in Fig. 1. The reservoirs contain water molecules and Na$^+$, K$^+$, or Ca^{2+} cations, as well as Cl$^-$ anions, at concentrations of about 1 mol/l. Water molecules interact via the "extended simple point-charge" (SPC/E) model potential,[18] which involves a Lennard-Jones (LJ) potential between the oxygen (O) atoms, and Coulombic interactions between sites associated with the O atoms (charge $-2q$) and two H atoms (charge $+q$). The values of the LJ potential parameters ϵ and σ are listed in Table I, while the electric charge is $q = 0.428e$. The water molecules are rigid and nonpolarizable, with an OH bond of 1 Å, and an HOH bond angle of 109.5°. The ions interact via the Coulomb potential and a LJ potential with each other and the water O atoms; we used the ion LJ parameters of Spohr,[19] summarized in Table I. Ion cross terms are calculated by the usual Lorentz–Berthelot combining rules. The LJ parameters are the same as those used by Lee and Rasaiah[20] and Lynden-Bell and Rasaiah[21] for the calculation of the mobilities of ions in bulk water and in infinitely long cylindrical channels, as well as in the work of Chung et al.[15] in BD simulations of ion channels. Water O atoms interact with the planar membrane surfaces (wall) by a potential of the 9-3 form,

$$V_w(z) = 4\epsilon'[(\sigma'/z)^9 - (\sigma'/z)^3],\tag{1}$$

where z is the distance of the O atom center from the planar surface, and the parameters ϵ' and σ' are given in Table I.

This potential is the same as that used for the simulation of liquid water between hydrophobic surfaces by Lee et al.,[22] and is obtained by the integration of the water-hydrocarbon LJ interaction over an infinite wall. The same LJ potential is integrated over the volume confining an infinitely long cylindrical cavity to determine the radial interaction potential $V_p(r)$ between the pore surface and the particles inside the cylindrical pore.[23] An interpolation procedure, described in Appendix A, is applied at the pore edges to avoid any discontinuities. A similar procedure is used to determine the surface-ion potential, and the resulting parameters of the 9-3 potential are summarized in Table I. The confining membrane is assumed to be nonpolarizable (i.e., constitutes a medium of dielectric permittivity $\epsilon = 1$). The simulation setup and interactions are similar to those of Allen et al.,[10] which explored equilibrium fluctuations of water in such a pore, in particular, the intermittent filling and dewetting. Those simulations showed that membrane polarizability, characterized by a permittivity $\epsilon > 1$, does not significantly alter the observed behavior of confined water.

If R_p is the geometric radius of the cylindrical pore, one may conveniently define an effective radius R relative to the water molecules by the radial distance from the cylinder axis at which the interaction energy of a water O atom with the confining surface is zero. At room temperature, this leads to $R \simeq R_p - 2.5$ Å; similarly the effective length of the pore is $L \simeq L_p + 5$ Å (cf. Fig. 1). Most simulations were carried out for $L_p = 10$ Å ($L = 15$ Å) and the radius R_p was varied between 5.5 and 8.5 Å. These pore dimensions are comparable to those of the selectivity filter of many ion channels.

The MD simulations were carried out with the DLPOLY2.13 package,[24] using the Verlet algorithm[25] for the integration of the coupled equations of motion of all particles, with a time step of 2 fs. Electrostatic interactions between particles in the periodically repeated simulation box were calculated using the smooth particle-mesh Ewald method.[26] The overall pressure in the reservoirs was maintained at $P = 1$ bar and the temperature at $T = 300$ K with the

help of a Berendsen barostat and thermostat.[27]

III. WATER PERMEATION OF A NARROW PORE

In this section we consider the permeation of the model defined in Sec. II by pure water, first in the absence of any ions, and next under the influence of a strong axial electric field induced by a cation concentration gradient across the membrane.

A. Intermittency

Several authors have reported the intermittent filling of narrow hydrophobic pores by water, characterized by stochastic wetting/dewetting transitions between filled ("liquid") and empty ("vapor") states of the pore, on a nanosecond time scale.[5–10] Below a threshold value of the pore radius R_p for a given pore length L_p, water cannot permeate the hydrophobic pore, even though the critical effective radius R is typically more than twice the radius of a water molecule; in other words the empty (vapor) state is the only stable state.[10] A simple phenomenological, macroscopic explanation of this behavior was given by Allen *et al.*[10] and Beckstein and Sansom.[8] The free-energy cost of the rearrangement of the water molecules in the liquid state close to the pore surface can be estimated as the product of the surface tension γ and the area of the surface. This loss in free energy competes with that for creating two liquid-vapor interfaces at the two pore mouths when the latter is empty. The "bulk" pressure term being negligibly small for water under ambient conditions, the free-energy difference between the filled and empty states of a cylindrical pore of effective radius R and length L_p reads

$$\Delta\Omega = 2\pi R^2 \gamma - 2\pi R L_p \gamma_c, \tag{2}$$

where γ_c is the liquid-wall and γ the liquid-vapor surface tension. Note that L_p rather than L was chosen in Eq. (2), because the simulations for empty pores suggest that both liquid-vapor interfaces are, on average, located immediately at the cylinder endings. When $\Delta\Omega=0$, the empty and filled states are equally probable, and this defines the critical effective radius

$$R_c = L_p \gamma_c / \gamma. \tag{3}$$

To determine R_c for a pore of bare length $L_p=10$ Å, we have carried out extensive MD simulations for several values of the effective radius, 3.0 Å $\leqslant R \leqslant 6.0$ Å. The simulations were performed for periodic boxes of dimensions $L_x=L_y=24.1$ Å, and $L_z \simeq 52$ Å parallel to the pore axis. The temperature and pressure were maintained at the values $T=300$ K and $P=1$ bar, by coupling the system to a Berendsen thermostat, and a barostat which allowed box rescaling only in the z direction. The total number of water molecules in the simulation box was $N=740$.

We have computed the water occupancy, i.e., the number of water molecules within the pore, as a function of time, along trajectories in phase space extending over $T_{\text{sim}} \gtrsim 50$ ns. Results for three pore radii shown in Fig. 2 exhibit typical intermittent behavior, with a stochastic succession of empty and filled states; in the latter case the number N_w of
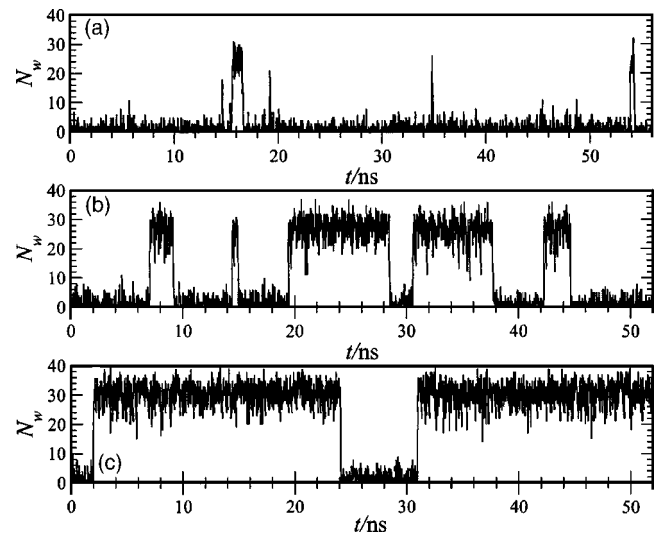

FIG. 2. Water occupancy in the pore N_w vs time t in nanoseconds for a pore of length $L_p=10$ Å and radii (a) $R_p=7.5$ Å, (b) 7.75 Å, and (c) 8.0 Å.

water molecules inside the pore fluctuates around a mean number $\bar{N}_w \simeq 30$ when $R_p=8$ Å ($R=5.5$ Å), which corresponds to a mean mass density of water inside the pore close to the bulk value of 1 g/cm³, in agreement with the findings of earlier simulations.[10]

Following Beckstein and Sansom,[7] we define the "openness" ω of a pore by

$$\omega = \frac{1}{T_{\text{sim}}} \int_0^{T_{\text{sim}}} dt \, \omega(t), \tag{4}$$

where the characteristic function $\omega(t)=1$ in the filled state ($\rho \approx \rho_0$ in the pore) and $\omega=0$ in the empty state ($\rho \approx 0$ in the pore). The threshold radius R_c is defined as the pore radius for which $\omega \simeq 0.5$. Although the total simulation time of $T_{\text{sim}}=50$ ns is clearly too short for the radius $R_p=8.0$ Å to observe a sufficient number of "flips" between filled and empty states [cf. Fig. 2(c)], we estimate the openness ω to be 0.04, 0.40, and 0.82 for effective radii $R=5.0$, 5.25, and 5.5 Å, respectively. This suggests a value of $R_c \simeq 5.3$ Å for the critical effective radius, which is close to earlier estimates based on shorter runs or more realistic hydrophobic channel models.[8] Substituting $R_c=5.3$ Å into Eq. (2), we obtain the estimate $\gamma_c \simeq 0.53\gamma$. The contact angle θ in Young's equation $\gamma_{vc} - \gamma_c = \gamma \cos\theta$ is then estimated to be $\theta \simeq 122°$, by assuming the vapor/channel surface tension γ_{vc} to be negligibly small and using the experimental value of $\gamma = 0.174 k_B T / \text{Å}^2$. The estimated contact angle is close to the measured value $\theta \simeq 118°$ for water on a flat methyl-terminated self-assembled monolayer.[28]

B. Electric-field effects

In our preliminary work[17] we have shown that an external electric field across the pore and embedding membrane generated by an imbalance of cation concentration in the reservoirs on both sides of the membrane has profound effects on water confined to a nanopore. We examine the structure, electrostriction, and dielectric behavior of confined water under these conditions in more detail in this subsection.
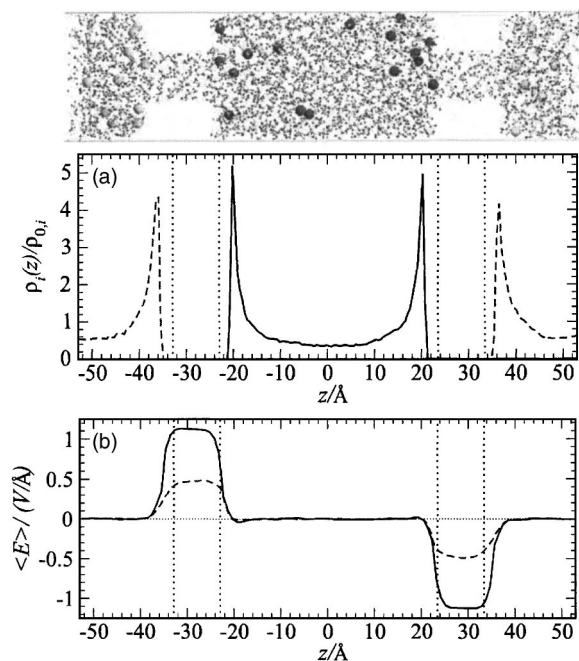
FIG. 3. Top frame: snapshot of the simulation setup with 16 ions in each reservoir. The dark spheres in the middle reservoir are ions with negative charge $-q$, the light spheres correspond to ions with positive charge q. Each reservoir contains a total charge $|Q|=16q$. The other particles are SPC/E water molecules. (a) Average density profiles $\rho_i(z)$ of the anions and cations in the reservoir normalized by their bulk densities $\rho_{i,0}$. (b) Averaged electric field $\langle E \rangle$ along the z axis measured in a pore of radius $R_p=7.0$, without water (solid line) and with water (dashed line). The dotted vertical lines mark the position of the slab surfaces. The mean field in the pore is $\langle E_0 \rangle \simeq 1.12$ V/Å without water and $\langle E \rangle \simeq 0.46$ V/Å with water.

The simulation setup is sketched in Fig. 3. Since the reservoirs on both sides of the membrane have different concentrations of anions and cations, periodic boundary conditions in the z direction require the basic cell to contain two pores in succession, say A and B. The reservoir to the right of pore A is also the reservoir to the left of B, and vice versa. In this part of our investigation which focuses on equilibrium properties of pore-confined water in a strong electric field, we add 16 anions (Cl$^-$) of (partial) charge $-q(0 \leq q \leq e)$ to one reservoir and 16 cations (Na$^+$) of (partial) charge $+q$ to the other reservoir. In order to maintain the overall system in a stationary state, the pore is made impermeable to the ions by setting the pore radius to zero only for the latter, thus preventing a net flow of ions (i.e., an electric current), and consequently a gradual drop in voltage. The relaxation towards equilibrium when the pore is open to ions will be examined in Sec. V. Due to the mutual repulsion of equally charged ions in one reservoir and the attraction to oppositely charged ions in the other reservoir, ions tend to condense symmetrically near the membrane surfaces leading to condenserlike configurations. This is illustrated by the concentration profiles of anions and cations shown in Fig. 3(a). The profiles on both sides of the two membrane slabs are not symmetrical, due to the different sizes of anions and cations, and the differences in their interactions with walls, water, and other ions. Local electric fields are measured as explained in Appendix B. Examples of the mean axial field $\langle E(z) \rangle$ (field component along Oz resolved in z) are shown in Fig. 3(b). By $\langle .. \rangle$ we denote the radial

average over the water accessible volume ($r < R$ inside the pore) at a given position z. As expected, the electric field vanishes in the conducting reservoirs, as a consequence of ion mobility, while it is substantial and almost constant inside the pores with opposite signs in A and B. The field strength can be adjusted by varying q. Examples of axial electric-field profiles observed when $q=0.446\,25e$ (i.e., total charges $Q=\pm 7.14e$ in the reservoirs) are shown in Fig. 3(b), for a pore radius $R_p=7.0$ Å. The mean value of the electric field $\langle E_0 \rangle = 1/L_p \int_0^{L_p} \langle E_0(z) \rangle dz$ inside pores empty of water is found to be surprisingly close to the value expected for a condenser of surface-charge density $\tau = Q/(2L_x^2)$, with $L_x = 24.1$ Å (the lateral size of the slabs), namely, $E_0 = \tau/\epsilon_0 \simeq 1.12$ V/Å. When the pore is filled with water, the electric field inside is reduced by the opposing polarization field. With the same physical parameters, we now find a mean value $\langle E \rangle \simeq 0.46$ V/Å, as shown in Fig. 3. Note that in the absence of the electric field, a pore radius $R_p=7.0$ Å ($R = 4.5$ Å) would be empty of water as shown in the previous section, or in the work of Allen et al.[10] A qualitative, macroscopic analysis of the critical field required to fill a hydrophobic pore of given radius and length will be given at the end of this section.

Although a dielectric permittivity ϵ is an ill-defined concept in nanometer scale-confined polar fluids,[29] where it is, for the least, a tensorial quantity, one may attempt to use two alternative macroscopic definitions of ϵ to characterize dielectric screening within the pore. On one hand ϵ may be defined as the ratio of the average fields within the empty ($\langle E_0 \rangle$ or "applied field") and filled ($\langle E \rangle$ or "screened field") pore, i.e.,

$$\epsilon = \langle E_0 \rangle / \langle E \rangle. \tag{5}$$

The average local permittivity in the pore can also be estimated from the mean polarization $\langle P \rangle$ according to

$$\epsilon_p = 1 + \frac{\langle P \rangle}{\epsilon_0 \langle E \rangle} = 1 + \frac{\rho \mu \langle \cos \theta \rangle}{\epsilon_0 \langle E \rangle}, \tag{6}$$

where $\mu = 7.841 \times 10^{-30}$ C m $= 0.489e$ Å is the dipole moment of a single SPC/E water molecule,[18] ρ is the mean number density inside the pore, and $\langle \cos \theta \rangle$ characterizes the mean orientation of the dipole vector of the molecules with respect to the z axis. According to elementary electrostatics, the two definitions (5) and (6) would yield identical results in the bulk.

By varying q in the MD simulations, one may now estimate the effective dielectric screening via Eq. (5) and the local permittivity from Eq. (6). The results for ϵ and ϵ_p, tabulated in Table II for several pore radii R, are seen to differ for every applied field, except in the bulk. The differences may be, at least qualitatively, understood from a simple macroscopic, electrostatic model described in Appendix C. The resulting total inhomogeneous electric-field distribution is illustrated in Fig. 4, for a pore geometry $R = 5$ Å and $L = 15$ Å. The curve shows the axial component $E(r, z=z_c)$ of the local electric field as a function of the radial distance r, at the center of the pore ($z = z_c$); the curve in the inset is the axial component along the pore axis $[E(z, r=0)]$

TABLE II. Properties of water confined to a cylindrical pore of length L_p $=10$ Å and diameter (a) $R_p=8.5$ Å, (b) $R_p=7.0$ Å, and (c) $R_p=5.5$ Å in an electric field $\langle E_0 \rangle$. (d) shows results from applied field simulations in bulk water under atmospheric pressure. $\langle E \rangle$ has an uncertainty of about 0.015 V/Å and could not be accurately determined for the smallest field ($\langle E_0 \rangle = 0.28$ V/Å) in (a) and (b).

	$\langle E_0 \rangle/$(V/Å)	$\langle E \rangle/$(V/Å)	ϵ	ϵ_p	$\langle \cos\theta \rangle$	ρ/ρ_0
(a)	0.28	⋯	⋯	⋯	0.51	1.10
	0.56	0.045	12.4	56.6	0.72	1.21
	0.84	0.119	7.1	29.3	0.84	1.42
	1.12	0.281	4.0	14.7	0.89	1.58
	1.67	0.601	2.8	8.7	0.95	1.88
(b)	0.28	⋯	⋯	⋯	0.77	1.12
	0.56	0.112	5.0	32.2	0.84	1.47
	0.84	0.278	3.1	16.6	0.90	1.75
	1.12	0.462	2.4	12.1	0.93	2.05
(c)	0.28	0.063	4.4	56.8	0.80	1.53
	0.56	0.266	2.1	18.8	0.87	1.97
	0.84	0.465	1.8	13.9	0.92	2.41
	1.12	0.682	1.7	10.6	0.94	2.63
(d)	2.05	0.05	40.1	40.1	0.67	1.00
	2.49	0.10	24.9	24.9	0.80	1.00
	3.10	0.25	12.4	12.4	0.91	1.01
	3.75	0.50	7.5	7.5	0.93	1.02

as a function of the coordinate z along the axis. The latter goes through a maximum at the center of the pore, and this maximum value goes over to the applied field E_0 as the distance from the axis increases. The results shown in Fig. 4 are in semiquantitative agreement with the simulation data shown in Fig. 5. The on-axis axial component $E(z, r=0)$ also goes through a maximum, but the curve is no longer symmetric around $z=z_c$, due to the molecular structure of the dipolar solvent. In the central plane $z=z_c$, $E(r, z=z_c)$ tends much more slowly to $\langle E_0 \rangle$ as $r \gg R$, which may reflect finite-size effects when approaching the edges of the simulation box.

When subjected to an applied electric field, water undergoes electrostriction and dielectric saturation.[2] In bulk water
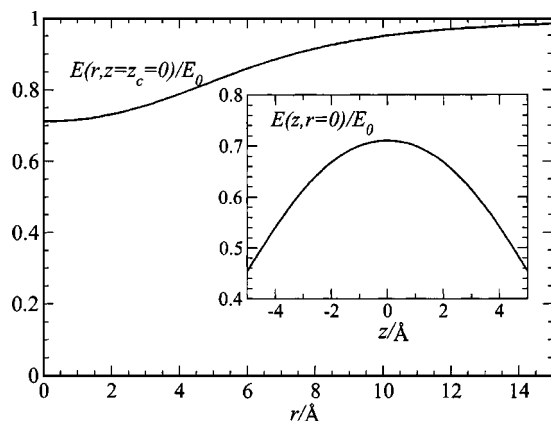
FIG. 4. Electric-field distribution from the simple macroscopic model described in Appendix C for a pore of geometry $R=5$ Å and $L_p=10$ Å. Plotted is the z component of the electric field in axial $E(z, r=0)$ and radial directions $E(r, z=z_c)$. Note that $z_c=0$ in this figure.
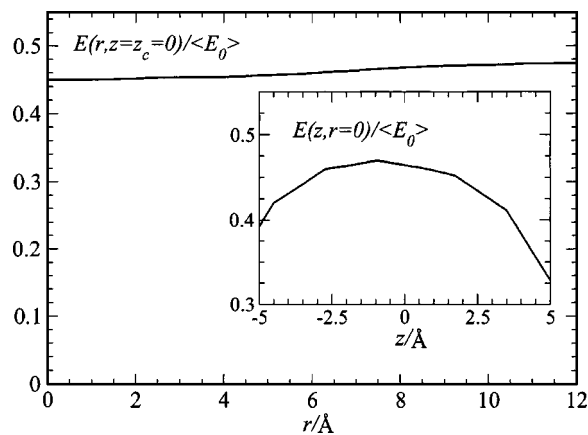
FIG. 5. Same as Fig. 4 but now for our simulation model with $R=4.5$ Å, $L_p=10$ Å, and $\langle E_0 \rangle = 1.12$ V/Å.

electrostriction is relatively weak, even under strong fields, i.e., the increase in overall density is at most a few percent. Due to the alignment of the molecular dipoles in the applied field, and the reduction in dipolar fluctuations, the dielectric permittivity decreases sharply, as shown in Table II. Except for the expected layering near the confining walls, the bulk behavior of water in an external field electric field is not significantly affected when water is confined between two plates (slit geometry), when the latter are several molecular diameters apart.[3] This behavior changes dramatically when water is confined to a narrow cylindrical pore. While in the absence of an applied electric field, the mean density of water remains close to its bulk value for radii sufficiently large to allow permeation of the hydrophobic pore (i.e., $R > R_c \simeq 5.3$ Å), considerable electrostriction is observed when a strong electric field is applied. Electrostriction increases with decreasing pore radius, and for radii below the zero-field threshold radius $R_c \simeq 5.3$ Å, water is driven into the pore by a sufficiently strong applied field. The mean water densities inside a pore of length $L_p=10$ Å (effective length $L=15$ Å) measured in our MD simulations are listed in Table II for three pore radii R_p (two of which are below the zero-field threshold) and for several electric fields. Electrostriction of more than 100%, i.e., a doubling of the bulk water density, is observed for the narrowest pore and the largest fields! The observed electrostriction is independent of the ensemble used, because the pore is connected to large reservoirs, so that constant volume (NVT) simulations show hardly any differences compared to NPT simulations at 1 bar. Table II also shows that electrostriction is accompanied by dielectric saturation, i.e., a reduction of the dielectric permittivity, which is significantly stronger than in the bulk, and strongest for the narrowest pore.

The strong electrostriction must be attributed to a significant distortion of the hydrogen bond network. This is quantified by calculating the probability distribution $P(n_{hb})$ of finding n_{hb} hydrogen bonds per molecule in the pore. We have used the geometric criterion for hydrogen bonds put forward in a recent paper[30] which investigated the structure of the first coordination shell in liquid water. Using configurations generated in the MD simulations we calculated the distribution $P(n_{hb})$ for bulk water and for water confined to
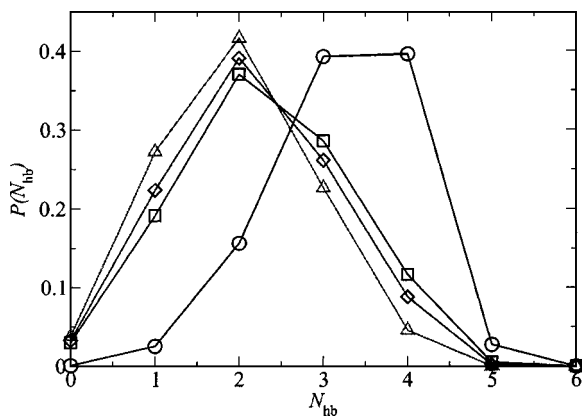
FIG. 6. Probability distribution P of the number of hydrogen bonds N_{hb} for SPC/E water in the bulk (circles), and confined to a narrow pore with radius $R_p=8.5$ Å (squares) and $R_p=7.75$ Å (diamonds). Also shown is the distribution for $R_p=5.5$ Å (triangle up) in an electric field $\langle E_0 \rangle=0.14$ V/Å.
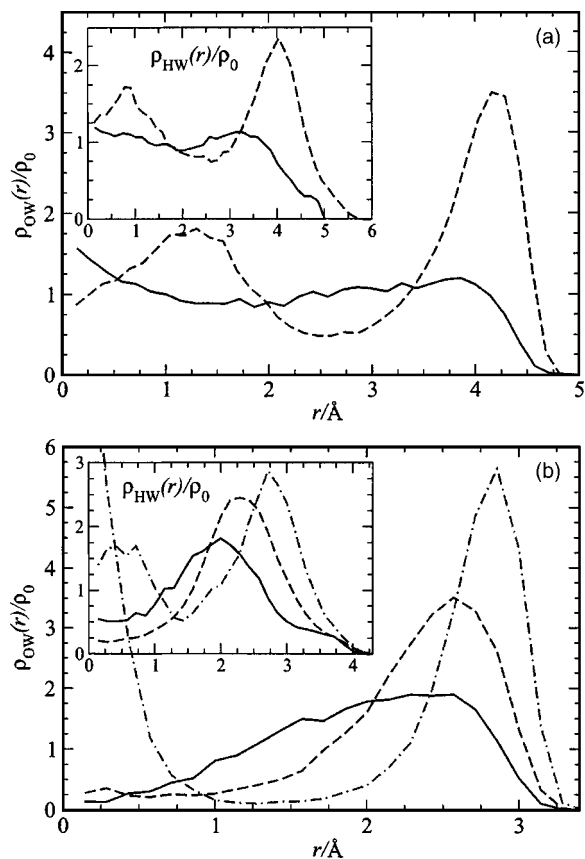

FIG. 7. Radial density profiles of water oxygen ρ_{OW} and hydrogen atoms ρ_{HW} (insets) in narrow cylindrical pores for radii (a) $R_p=7.0$ Å and (b) $R_p=5.5$ Å. In (a) the results for applied fields of $\langle E_0 \rangle=0.14$ and $\langle E_0 \rangle=0.56$ are shown. In (b) the fields are $\langle E_0 \rangle=0.28$ V/Å (solid line), $\langle E_0 \rangle=0.56$ V/Å (dashed line), and $\langle E_0 \rangle=0.84$ V/Å (dot-dashed line).

pores of radii $R_p=8.5$ and 7.75 Å, which are intermittently filled in the absence of electric field. For the narrowest pore investigated ($R_p=5.5$ Å), a field $\langle E_0 \rangle \simeq 0.14$ V/Å is required for the channel to fill. The resulting distributions $P(n_{hb})$ are shown in Fig. 6. The distribution is significantly shifted towards lower values of n_{hb} as the confinement increases. The measured average numbers of hydrogen bonds are $\langle n_{hb} \rangle=3.24$ in the bulk, $\langle n_{hb} \rangle=2.28$ and 2.16 for $R_p=8.5$ and 7.75 Å (in the absence of external field), and $\langle n_{hb} \rangle=1.97$ for $R_p=5.5$ Å with an electric field $\langle E_0 \rangle=0.14$ V/Å.

The change of local structure with electric field can also be seen in the oxygen and hydrogen radial density profiles in the pores shown in Fig. 7. Frame 7(a) corresponds to a pore radius $R_p=7.0$ Å. For the smallest applied field, $\langle E_0 \rangle=0.14$ V/Å, the two density profiles are rather flat, and close to the bulk density of water, as already noticed in the equilibrium simulations of Allen *et al.*[10] An applied field $\langle E_0 \rangle=0.56$ V/Å, corresponding to a measured average field $\langle E \rangle=0.112$ V/Å inside the pore, leads to a strong layering of the water molecules, particularly near the cylindrical pore surface. The corresponding mean density of water is 47% higher than in the bulk (cf. Table II)! The profiles for the narrower pore with $R_p=5.5$ Å, measured for three fields of increasing amplitude $\langle E_0 \rangle$, are shown in Fig. 7(b). The layering and mean density increase dramatically with $\langle E_0 \rangle$. As expected, the hydrogen atoms can get closer to the pore surface. At the highest field a second water layer forms near the pore axis.

The electric-field-induced filling of narrow hydrophobic pores may be understood, at least qualitatively, in terms of macroscopic considerations. In the presence of an applied field E_0, the free-energy difference (2) between filled and empty states must be generalized to

$$\Delta \Omega = 2\pi R^2 \gamma - 2\pi R L_p \gamma_c + V \frac{\epsilon_0}{2} E_0^2 \left(\frac{1}{\epsilon_g} - \frac{1}{\epsilon_l} \right), \qquad (7)$$

where the third term is the electrostatic energy difference, assuming that the electric field inside the pore is homogeneous over the pore volume $V=\pi R^2 L_p$, and ϵ_g and ϵ_l are the permittivities of the confined water vapor or liquid, corresponding to the "empty" and "filled" states, respectively.

These two states are equally probable when $\Delta \Omega=0$, and thus the critical radius in the presence of an external field E_0 is given by

$$R_c = \frac{4 L_p \gamma_c}{4\gamma + \epsilon_0 \Delta \epsilon L_p E_0^2}, \qquad (8)$$

where $\Delta \epsilon = (1/\epsilon_g - 1/\epsilon_l)$, generalizes Eq. (3), and indeed shows that the critical radius R_c decreases with increasing field E_0. For a given pore geometry ($R<R_c, L_p$), Eq. (8) may be rewritten to express the critical field above which the pore fills

$$E_{0,c} = 2 \sqrt{\frac{L_p \gamma_c - R\gamma}{R L_p \epsilon_0 \Delta \epsilon}}. \qquad (9)$$

Since $\epsilon_l \gg \epsilon_g$, even in confined geometry, $\Delta \epsilon \simeq 1$. The critical field (9) is plotted versus the pore radius R for a pore length $L_p=10$ Å in Fig. 8; the experimental liquid-gas surface tension $\gamma=0.174 k_B T/\text{Å}^2$ is used, together with the relation $\gamma_c=0.53\gamma$ derived from our earlier analysis of the critical radius in the absence of the electric field [Eq. (3) and discussion at the end of Sec. III A]. Critical fields estimated from 50-ns MD simulations for three pore radii are shown in Fig. 8 for comparison. The theoretical estimate (9) is seen to exhibit the right trend, but to overestimate the measured critical fields by nearly an order of magnitude. There are at least three possible explanations for this quantitative discrepancy.
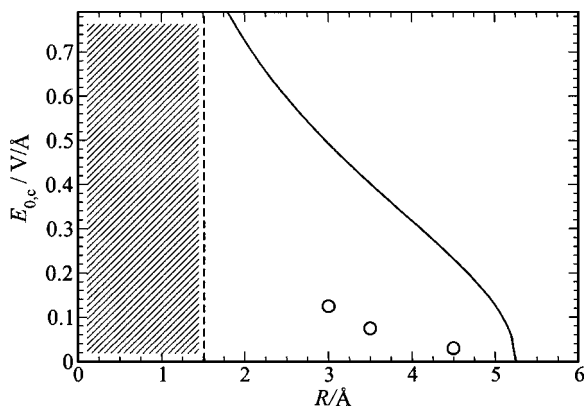
FIG. 8. Critical field $E_{0,c}$ vs the effective pore radius R for a fixed pore length $L_p=10$ Å. The channel is filled with water for fields larger than the critical field. We compare theoretical estimates from the phenomenological theory (9) to simulation results for $R=4.5$ Å, $R=3.5$ Å, and $R=3.0$ Å depicted as circles. The shaded region indicates pore radii smaller than one water radius $R \leqslant 1.5$ Å.

First, the macroscopic electrostatic model in Appendix C shows that the screened field in the filled pore is far from homogeneous, and extends to radii well outside the pore radius (cf. Figs. 5 and 6), so that a volume larger than the pore volume V should be considered for the electrostatic contribution in Eq. (7). Second, we have seen that finite-size effects in the simulations can modify the electric-field distribution significantly when moving radially away from the pore. Finally, the surface tensions γ and γ_c could change significantly under the action of the electric field due to the strong restructuring of the water molecules. The full explanation of the discrepancy between the macroscopic model and the simulation data might very well be a combination of these reasons.

IV. FREE-ENERGY PROFILES FOR ION PERMEATION

A single ion approaching the channel membrane faces a free-energy barrier which it must overcome for channel permeation. The origin of the barrier is twofold: first, confinement of the ion to a narrow pore strongly reduces the volume locally accessible to it, and thus lowers the configurational entropy; second, there is a cost in solvation free energy, since the ion is surrounded by fewer, and differently structured water molecules compared to the hydration shell in the bulk. We assume that both mechanisms are independent, and contribute additive components of a Landau free-energy profile which is a function of an "order parameter" z, the distance of the ion from the center of the pore along its axis,

$$F(z) = F_{\mathrm{conf}}(z) + F_{\mathrm{sol}}(z), \qquad (10)$$

where $F_{\mathrm{conf}}(z)$ is the entropic cost arising from the confinement, while F_{sol} is the solvation part. $F(z)$ may, in principle, be calculated, within a constant C, from the probability density $P(z)$ of finding the ion in the interval $[z, z+dz]$,

$$F(z) = -k_B T \log[P(z)] + C. \qquad (11)$$

$P(z)$ can be measured in simulations of the system sketched in Fig. 1, i.e., involving a pore through a membrane separating two reservoirs filled with water, and containing a single

ion, the position of which is monitored during a MD evolution to determine a histogram of the ion positions. This direct method faces, however, two problems: (i) on one hand an excessively long simulation would be required for the ion to sample representative positions in the reservoirs and within the narrow pore, in order to accurately determine the ratio of probabilities of finding the ion in the pore or in the reservoirs, and (ii) on the other hand the expected steep free-energy barriers at the two mouths of the pore entail vanishingly small probabilities for the ion to permeate the pore. Problem (i) is essentially entropic and concerns directly the confinement free energy F_{conf} in Eq. (10). The latter can be estimated from the "free" area $A_p(z)$ accessible to the ion at any given position z; it depends only on the size of the ion relative to the pore dimension, and is independent of ionic charge and water configuration. If L_x is the lateral dimension of the reservoirs (i.e., of the simulation box),

$$\beta F_{\mathrm{conf}}(z) = -\log\left[\frac{A_p(z)}{L_x^2}\right]. \qquad (12)$$

Obviously, the barrier depends on the lateral simulation box area; for a physical system this corresponds to the inverse pore density per unit area, given for instance by the ion channel surface density on a cell membrane.

Let z be the distance to the center of the pore z_c, conveniently chosen to be $z_c=0$. For positions along the axis outside the effective width of the membrane $|z|>L/2$, $A_p(z) = L_x^2$, while inside the cylindrical channel ($|z|<L_p/2$), $A_p(z) = \pi R_i^2$, where $R_i = R_p - \sigma_i'$ is the effective radius of an ion of species i (the wall ion interaction diameters σ_i' are listed in Table I. For $L_p/2 < |z| < L/2$, the effective radius is given by the smooth interpolation formula $R_i(z) = R_p - \sqrt{\sigma_i'^2 - (z - L_p/2)^2}$. For the box size $L_x = 24.1$ Å, used in our simulations, the barrier heights calculated from Eq. (12) vary typically between 1.5 and $4k_B T$, depending on the radius of the ion under consideration.

Once the contribution to the Landau free energy due to confinement has been determined from Eq. (12), the solvation part in Eq. (10) may be efficiently calculated by confining the ion to a cylindrical pore of radius equal to that of the membrane pore outside the latter, and spanning the whole simulation cell; due to the periodic boundary conditions, this means that the ion is confined within a pore of infinite length. In the reservoirs, this confinement will not affect the bulk solvation free energy, since the water molecules around the ion are still free to move and rotate in and out of the extended pore. The probability density of finding the ion at z, under the infinite pore constraint, will be referred to as $P(z)$. Problem (ii) concerning the sampling of ion configurations near the steep potential barriers may then be overcome by a variant of "umbrella sampling,"[25] whereby the ion (but not the water molecules) is subjected to a biasing potential $B_{z_0}(z)$ which forces the ion to sample a low probability region around a prescribed position z_0. The solvation part of the free energy (10) may then be extracted from the simulation by the following relation:
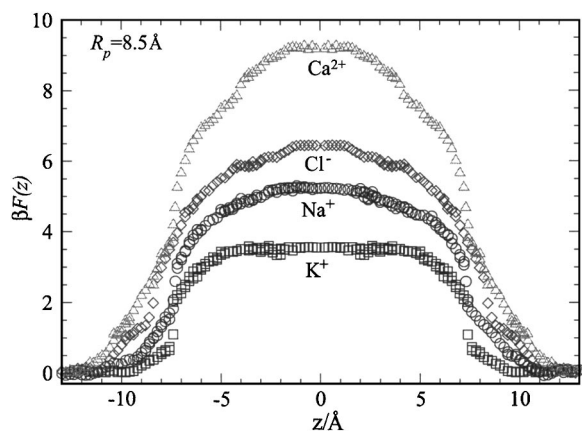
FIG. 9. (a) Free-energy barrier profiles $F(z)$ for K$^+$, Na$^+$, Cl$^-$, and Ca^{2+} ions permeating a channel with radius $R_p = 8.5$ Å and length $L_p = 10$ Å. Note that the center of the pore $z_c = 0$ in this figure.

$$F_{sol}(z) = -k_B T \log \left[\widetilde{P}(z) \right] - B_{z_0}(z) + C_{z_0}, \qquad (13)$$

where $\widetilde{P}(z)$ is now the probability distribution observed under the infinite pore constraint and in the presence of the biasing potential, and C_{z_0} is a constant depending only on the biasing potential. By choosing a range of biasing potentials $B_{z_0}(z)$, one can explore the whole range of positions z; the overlaps of the resulting $F_{sol}(z)$ allow C_{z_0} to be determined over the whole range of positions. A similar method has recently been used to determine the free-energy profiles of water inside narrow pores.[10] We have chosen a simple parabolic biasing potential of the form

$$B_{z_0}(z) = k(z - z_0)^2, \qquad (14)$$

with values of the spring constant k in the range of $1-10$ kJ mol^{-1} Å^{-2}.

Results for the total free-energy profile, i.e., the sum of the contributions (12) and (13), are plotted in Fig. 9 for K$^+$, Na$^+$, Cl$^-$, and Ca^{2+} ions, and a pore of length $L_p = 10$ Å (effective length $L = 15$ Å), and radius $R_p = 8.5$ Å ($R = 6.0$ Å). The barriers are obviously symmetric and their rise starts already at $z \simeq \pm 10$ Å, i.e., well before the ion reaches the pore mouth on either end. Inside the pore, the profiles exhibit flat maxima of height approximately equal to 3, 5, 6.5, and $9.5 k_B T$ for K$^+$, Na$^+$, Cl$^-$, and Ca^{2+} ions, respectively. The order of the increasing barrier heights correlates well with the decrease in solvation free energy of the ions in bulk SPC/E water.[31] Note that the larger K$^+$ ion experiences a lower potential barrier than the smaller Na$^+$ ion, and is less preferentially solvated than the latter. The data shown in Fig. 9 and the results of Lynden-Bell and Rasaiah[31] allow the qualitative conclusion that stronger solvation in the bulk leads to a higher barrier upon confinement of the ion to a narrow pore. However, when the pore radius decreases to a value comparable to the ion radius, $A_p(z)$ goes to zero and the confinement free energy (12) diverges, and hence dominates the solvation contribution for sufficiently narrow pores.

In the case of the narrowest hydrophobic ion channels, we have seen that the pore "dries," and an axial electric field is required to drive water molecules inside. In order to calculate the free-energy barrier to ion permeation in that case,
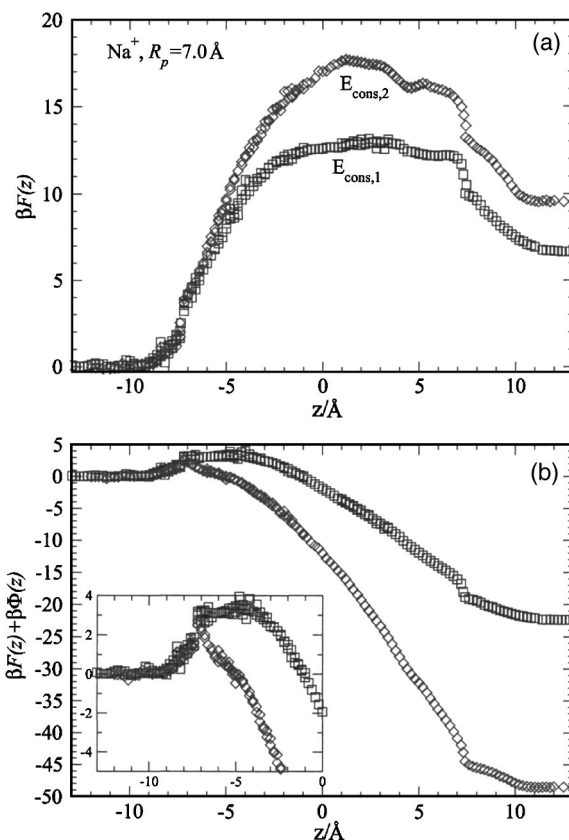

FIG. 10. (a) Free-energy barrier profiles $F(z)$ for Na$^+$ in a pore of radius $R_p = 7.0$ Å, with a constraining field $E_{cons,1} = 0.05$ V/Å (squares), and $R_p = 7.0$ Å with a constraining field $E_{cons,2} = 0.1$ V/Å (diamonds). The constraining field keeps the narrow channel filled with water. (b) The total free energy including potential (15) for Na$^+$ in a $R_p = 7.0$-Å pore, for constraining fields as in (a). The inset shows a magnification of the profile near the pore entrance for a better identification of the barrier height.

we have used a constraining potential acting on the water molecules alone, and mimicking the "condenser" setup described in Sec. III B. The chosen potential acts only on the water oxygen and hydrogen atoms in the interval $|z| < L/2$, i.e.,

$$\Phi(z) = \begin{cases} 0 & \text{for } z < -L/2, \\ -E_{cons} q_i z & \text{for } |z| \leq L/2, \\ -E_{cons} q_i L & \text{for } z > L/2, \end{cases} \qquad (15)$$

where E_{cons} is the magnitude of the constraining field. The constrained probability distribution $\widetilde{P}_B(z)$ in Eq. (13) is now calculated with the additional constraint on the water molecules arising from (15).

The resulting Landau free energy for a Na$^+$ ion near a pore of length $L_p = 10$ Å and $R_p = 7.0$ Å is plotted in Fig. 10(a) for two constraining fields $E_{cons} = 0.05$ and 0.10 V/Å. By convention the free energy is set to zero in the left-hand reservoir; the calculated profiles are now highly asymmetric. This may be understood as follows. The constraining field E_{cons} polarizes the water inside the pore, inducing "surface" charges at the two ends of the pore, which in turn generate a reaction field. The latter increases with E_{cons} and acts on the ion. The magnitude of this induced field can be estimated from the total free-energy gain of the ion after permeation,

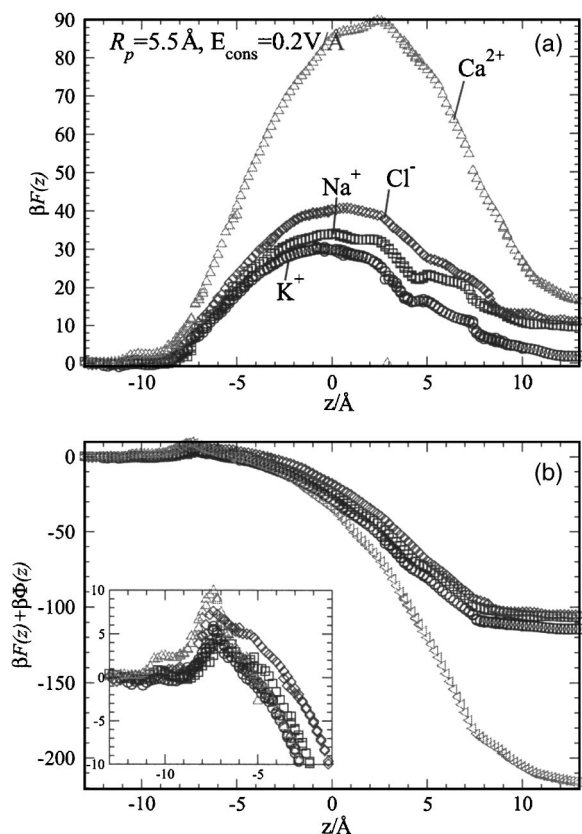FIG. 11. (a) Free-energy profiles $\beta F(z)$ for K$^+$ (squares), Na$^+$ (circles), Cl$^-$ (diamonds), and Ca^{2+} (triangles) ions permeating a channel with radius R_p =5.5 Å, with a constraining field E_{cons}=0.2 V/Å. (b) The same as (a) but now the potential (15) is included. The inset shows a magnification of the profiles for a better identification of the barrier height near the pore entrance.

divided by the channel length and the ion charge q, i.e., $E_{ind} \simeq [F(z=L/2)-F(z=-L/2)]/(Lq)$. This yields E_{ind} $\simeq 0.013$ and 0.018 V/Å for E_{cons}=0.05 and 0.1 V/Å. The small structure observed in $F(z)$ around $z=5$ Å (but absent at $z=-5$ Å) is probably a signature of the asymmetric solvation of the ion by oriented water molecules close to the pore endings.

Figure 10(b) shows the free-energy profiles when the potential (15) also acts on the ion, as is the case in the setup of Fig. 3, which will be used in Sec. V to investigate the relaxation of an initial ion concentration gradient across the membrane to equilibrium. The free-energy profiles are now dominated by the contribution of the applied field, and the barrier height is nearly suppressed. The remaining barrier near the left-hand pore entrance is less than $4k_BT$ for the lower applied field and about $2k_BT$ for the higher E_{cons}, in the case of Na$^+$.

Free-energy profiles for the four ionic species K$^+$, Na$^+$, Cl$^-$, and Ca^{2+} are compared in Fig. 11 for the narrow channel of radius R_p=5.5 Å. A field of magnitude E_{cons}=0.2 V/Å is applied to ensure that the pore is filled with water; this is a magnitude comparable to that achieved in the nonequilibrium simulation in Sec. V. The mirror image of the density profile of the anions Cl$^-$ is shown to allow comparison with the cation results. The barriers in Fig. 11(a), where the ions are not subjected to the potential (15), are ordered as for the wider pore (cf. Fig. 9). The total free-energy offset $F(z$

$=L/2)-F(z=-L/2)$ is different for the four species, showing that the induced fields, which would be identical in the absence of ions, are sensitive to the charge and the size of the ions. The profiles corresponding to the case where the ions are also subjected to the potential (15) are shown in Fig. 11(b). The remaining barrier at the left pore entrance is largest for the Ca^{2+} ion ($\simeq 10k_BT$) as expected since this divalent cation is more strongly hydrated in the bulk than the monovalent ions.

We have also computed the free-energy profile of a Na$^+$ ion in a narrow channel (R_p=7 Å) empty of water (water permeation is prevented by setting the channel radius equal to 0 for the water molecules). The barrier turns out to be extremely high [$F(z=z_c) \simeq 108k_BT$], in good agreement with the absolute value of the solvation free energy of Na$^+$ in bulk SPC/E water,[31] showing that the ion permeation of a pore empty of water is extremely unlikely, even when it is as short as 1 nm.

V. RELAXATION TO EQUILIBRIUM

We now turn to the physiologically important situation of an initial charge imbalance across the membrane, corresponding to different anion and cation concentrations in the reservoirs separated by the membrane. In order to allow the implementation of periodic boundary conditions in the z direction, the setup involving two membranes, sketched in Fig. 3, has been used in these nonequilibrium MD simulations. All ions carry their physical charges. One reservoir has initial concentrations $c_+ \simeq 0.9M$ (12 cations) and $c_- \simeq 0.6M$ (8 anions), while in the second reservoir $c_+ \simeq 0.3M$ (4 cations) and $c_- \simeq 0.6M$ (8 anions). The cations were Na$^+$ or K$^+$, while the anions were always Cl$^-$. This initial charge imbalance generates an average electric field of 0.32 V/Å across the membrane, which is about one order of magnitude larger than under normal physiological conditions, but could be achieved in the course of a rare but large fluctuation at the pore entrance. The large cation concentration is necessary to improve the signal-to-noise ratio in the simulation. In the case of the divalent cation Ca^{2+} we chose a setup with the same Ca^{2+} concentration but twice the Cl$^-$ concentration to ensure electroneutrality. The dimensions of the total simulation cell including both channels are $L_x=L_y=23.5\pm0.3$ Å and $L_z=100.3\pm1.7$ Å with 1370 water molecules at P =1 bar and T=300 K. Each simulation was repeated at least ten times with different initial configurations, in order to gather sufficient statistics for the permeation events. In the setup of Fig. 3, with one reservoir in the middle and the other reservoir on both ends of the simulation cell along Oz, the concentration gradients, and hence the electric fields, are antiparallel in the two channels, and so will be the resulting ion currents. The relaxation towards equilibrium, where the two reservoirs are separately electroneutral, thus involves an indirect coupling of the two pores.

The nonequilibrium simulations were carried out for an effective pore radius R=3 Å, which, in the absence of the electric field due to the charge imbalance, would be closed to water. Under the initial conditions of the nonequilibrium runs, the pore spontaneously fills with water, since the elec-
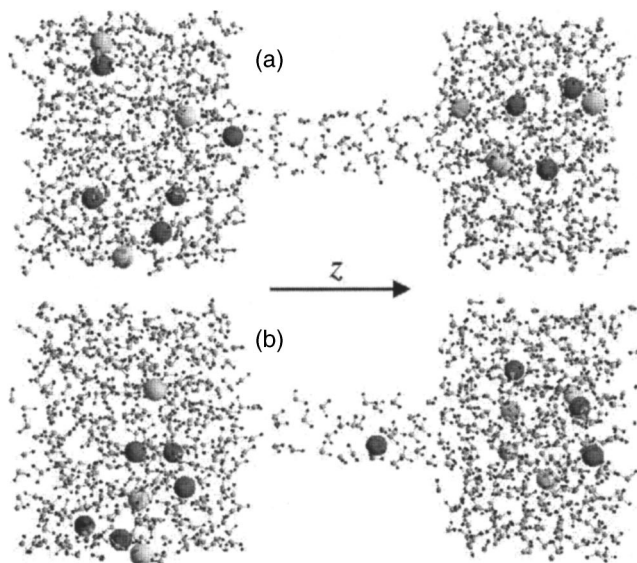
FIG. 12. Simulation snapshots. Molecular configurations (a) before a cation (dark gray spheres) permeates the channel and (b), 10 ps later, while it goes through. Anions are shown as light gray spheres. Only half of the periodically repeated simulation cell is shown.
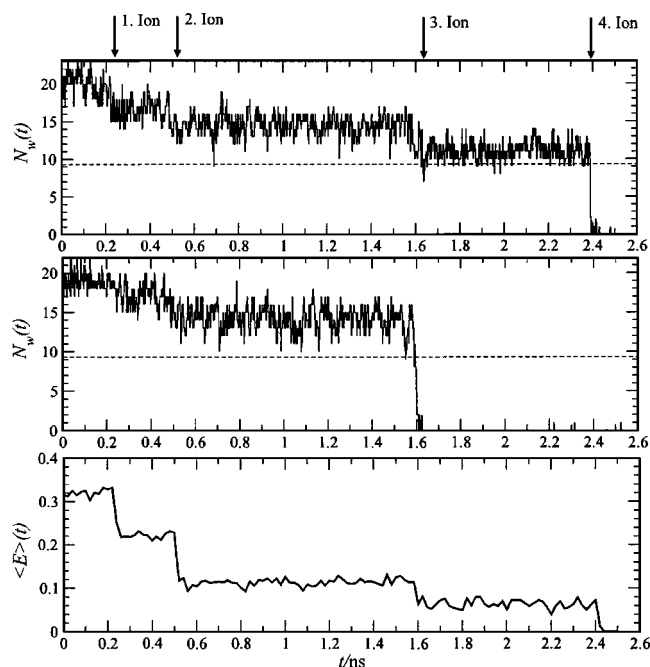

FIG. 13. First and second frames: water occupancy N_w vs time t from a typical nonequilibrium simulation (with Na$^+$ ions) in the left and right pores. The pore length is $L_p = 10$ Å and the pore radius is $R_p = 5.5$ Å ($R = 3$ Å). The times when ions cross the pores are indicated by the arrows above the upper frame. The number of water molecules in the pore, assuming bulk density N_{bulk}, is indicated by a dashed line. The third frame shows the mean measured field in the pores vs time t, averaged over the absolute fields in both pores.

tric field exceeds the critical field for that radius (cf. Fig. 8). The runs with Na$^+$ and K$^+$ cations show qualitatively the same behavior. During the course of most simulations, four cations move successively through the pore. Snapshots of such an event are shown in Fig. 12. Only rarely (typically 1 in 10 events) is a Cl$^-$ crossing observed, which may be understood from the significantly higher potential barrier experienced by Cl$^-$ compared to the monovalent cations (cf. Fig. 11). Each of the ion crossings reduces the charge imbalance between the two reservoirs, and hence the electric field inside the pore. The number of water molecules inside both pores, and the electric field averaged over each pore are plotted versus time in Fig. 13 for a typical simulation run involving Na$^+$ ions. Due to the strong electrostriction effect, already discussed in Sec. III B under equilibrium conditions, the number of water molecules is significantly larger than that expected from the bulk density, namely,

$$N_{bulk} = \rho_0(\pi R^2 L_p). \tag{16}$$

At each ion crossing the number $N_w(t)$ of water molecules drops sharply, while remaining above N_{bulk}. Once the third ion has crossed the first pore, after $t \simeq 1.6$ ns, the residual electric field is no longer strong enough to sustain the filled state, and the pore spontaneously empties of water. Thereafter the pore is impermeable to ions, as may be expected from the very high free-energy barrier of an empty pore, mentioned at the end of the previous section. The other pore in the simulation cell remains filled, however, and the final ion crossing eventually occurs through that pore which thereafter also empties of water, at which stage the total system has returned to equilibrium. The same behavior, involving the closing of one channel after the passage of the third ion, was observed in all ten simulations carried out with different initial conditions.

In simulations where equal numbers of cations of the two species Na$^+$ and K$^+$ are included, it is found that cross-

ing events are about twice as probable for the K$^+$ species than for the smaller Na$^+$ ions, which may be expected from the lower free-energy barrier experienced by the former ion (cf. Fig. 11).

Ion transport through a pore is found to occur essentially at constant velocity, as illustrated in Fig. 14, where the z coordinate of the permeating ion is plotted as a function of time. In the reservoirs, anions and cations undergo diffusive motion among the water molecules, characterized by a linear increase of the mean-square displacement with time. When a cation in the cation-rich reservoir comes close to the pore
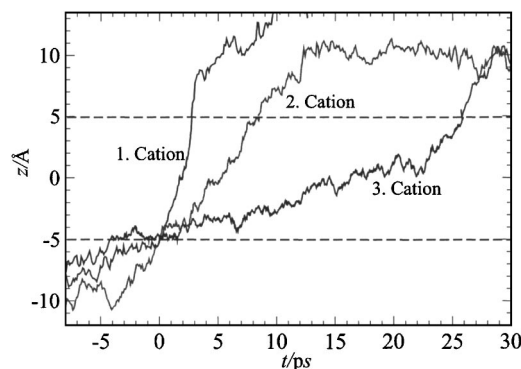

FIG. 14. Cation trajectories inside the pore and in its vicinity vs time t in picoseconds. The z coordinate of the cations is plotted vs time for three successive permeations in one typical simulation run. The cylindrical pore is located between $z = -5.0$ Å and $z = 5.0$ Å marked by the two long dashed lines. $t = 0$ defines the time at which the ions are located at the entrance of the pore.

TABLE III. Internal electric field $\langle E \rangle$, mean velocity v, and mobilities μ_+ of Na^+, K^+, and Ca^{2+} ions during the first, second, and third ion passages.

Ion	$\langle E \rangle/(V/Å)$	$v/(Å/ps)$	$\mu_+/(s\ kg^{-1})$
Na^+	0.32	2.3	4.5
Na^+	0.22	1.3	3.7
Na^+	0.11	0.4	2.3
K^+	0.32	5.9	11.5
K^+	0.22	3.6	9.2
K^+	0.11	0.6	3.4
Ca^{2+}	0.47	3.3	2.2
Ca^{2+}	0.39	2.5	2.0

mouth, it experiences the strong axial electric field pictured in Fig. 3, and is dragged into the channel. Analysis of ion passages in ten independent simulations run with the same initial charge imbalance, but different initial positions of the ions, shows that once an ion has penetrated inside the channel it moves with roughly constant velocity, estimated from the slope of the trajectories shown in Fig. 14. These slopes are approximately the same in all ten runs. The ion motion reverts to diffusive once it leaves the pore at the other end. The slopes observed for the first, second, and third ion crossings decrease, due to the drop in the driving electric field after each crossing. The slopes give direct access to the cation mobilities μ_+ via the constitutive relation $v=\mu_+ qE$, and the electric field measured inside the pore. The resulting values for Na^+, K^+, and Ca^{2+} averaged over ten runs with different initial configurations are summarized in Table III.

The measured mobilities are seen to increase with increasing field, but to remain of the same order of magnitude as the corresponding bulk mobilities (μ_+=5.1 and 8.4 s/kg for Na^+ and K^+, respectively).[20] The mobilities are, however, systematically larger than those deduced from the diffusion coefficients in infinitely long pores of the same effective radius (μ_+=1.2, 2.0, and 0.08 s/kg for Na^+, K^+, and Ca^{2+}, respectively).[21] This enhancement of the mobility must be attributed to the change of the structure of water inside the pore, due to the strong electric field (cf. Fig. 7).

We have checked the size dependence of our results by carrying out simulations in a larger box, by doubling the area of the x-y section, keeping the ion concentration gradient constant. As a consequence the numbers of water molecules and ions were doubled as well, so that twice the number of ion passages was required before the system relaxed to equilibrium. The jumps in the internal electric field and in the numbers of water molecules inside the pore upon an ion passage are thus smaller in this case than those shown in Fig. 13. Qualitatively similar behavior is observed upon varying the pore radius or length, except for the fact that for effective pore radii $R \gtrsim 5.3$ Å, the pore remains mostly filled with water even in the absence of an electric field.[10]

VI. CONCLUSIONS

We have combined a highly simplified generic model of hydrophobic pores with a semirealistic description of water and ions to investigate pore permeation by water molecules and cations under equilibrium and out-of-equilibrium condi-

tions by MD simulations. The dimensions (radius R and length L) of the cylindrical pore are comparable to those of the selectivity filter of many ion channels, or of segments of carbon nanotubes, but the model totally neglects the chemical structure of the confining pore surface. We have focused on the effects of varying the pore radius, and of the electric field on water and ion permeation for a fixed pore length L_p=1 nm (corresponding to an effective length L=1.5 nm). The key findings of the present work may be summarized as follows:

(a) The present simulations, which extend over at least 50 ns, confirm the intermittent filling of the hydrophobic cylindrical pore by water under equilibrium conditions, provided the pore radius exceeds a critical value $R_c \simeq 5.3$ Å, as reported earlier for the same model,[10] or for more realistic models of ion channels[6–9] or carbon nanotubes.[5] The critical radius agrees well with the prediction of a simple macroscopic calculation with reasonable values of the liquid/vapor and liquid/pore surface tensions [cf. Eq. (3)].

(b) Below the critical radius R_c water still permeates the pore under the action of a strong electric field. The electric field is produced in a condenserlike setup, whereby the reservoirs in both sides of the pore contain ions of opposite charge. Equilibrium conditions are mimicked by preventing the ions from passing through the pore to restore electroneutrality in the two reservoirs. The water driven into the channel exhibits strong electrostrictive behavior, as characterized by layered radial density profiles, a mean density up to twice the bulk density, and a dramatic drop in dielectric permittivity. All these observations can be traced back to a considerable distortion of the hydrogen-bond network inside the pore. The variation of the critical radius R_c with electric field is qualitatively, but not quantitatively reproduced by a macroscopic calculation of the competition between capillary and electrostatic contributions to the free-energy difference between filled and empty states in the pore.

(c) The free-energy barrier to ion permeation of a filled pore has been estimated by calculating the Landau free-energy profile as a function of the axial (z) position of a single ion. This free energy has an entropic contribution, due to confinement, which is easily calculated, and a solvation contribution, which must be estimated in the MD simulations with the help of a biasing potential (umbrella sampling). The latter contribution correlates well with known solvation free energies in bulk water. In particular, the barrier to entering the hydrophobic pore is lower for the K^+ than for the Na^+ ion. When the pore radius $R<R_c$, water must be forced inside the pore, by applying a biasing potential, which polarizes the channel. If the biasing field does not act on the ion, the barrier height felt by the latter increases with field strength. When the electric field also acts on the ion, the potential barrier drops to a few $k_B T$.

(d) We have finally explored the relaxation towards equi-

librium, by starting the MD simulations with a large charge imbalance between the reservoirs on both sides of the pore and observing the successive passages of ions through the pore to restore charge neutrality. At each ion passage, the electric field across the channel drops, reducing the initial strong electrostriction, i.e., the mean density of water inside the pore. After a succession of drops, the pore closes to water, and hence to ion transport, thus providing a possible mechanism for voltage-dependent gating of hydrophobic pores. Since the critical electric field, below which the channel closes to water, depends on the pore radius and length, we might expect that water permeation of hydrophobic pores is strongly dependent on pore geometry.

Although clearly not directly applicable to any specific pore or ion channel, our results give clear indications of generic trends in water and ion permeation upon varying the characteristics of the pore geometry, and the applied electric field. Apart from the chemical specificity, the physically most important feature missing so far in our model is the polarizability of the water molecules and of the pore-embedding material (e.g., the protein in the case of ion channels or aquaporins). Work along these lines is in progress.

ACKNOWLEDGMENTS

APPENDIX A: WATER-WALL AND WATER CYLINDER INTERACTIONS

We assume that the membrane wall is a homogeneous assembly of methane CH_3 molecules, each of which interacts with the water oxygen at a distance r via the Lennard-Jones potential

$$V_{LJ}(r) = 4\epsilon \left[\left(\frac{\sigma}{r} \right)^{12} - \left(\frac{\sigma}{r} \right)^6 \right] \qquad (A1)$$

with $\epsilon = 0.8148$ kJ mol^{-1} and $\sigma = 3.75$ Å. Integration of (A1) over the membrane volume yields a potential of the 9-3 form

$$V_w(z) = 4\epsilon' \left[\left(\frac{\sigma'}{z} \right)^9 - \left(\frac{\sigma'}{z} \right)^3 \right], \qquad (A2)$$

where z is the distance between the planar confining surface and the center of the O atom and $\epsilon' = 1.2578$ kJ/mol and $\sigma' = 2.474$ Å. This potential is the same as that used for the study of liquid water between hydrophobic surfaces by Lee et al.[22] The ion-wall interactions have been obtained accordingly. In our simulations V_w is shifted and cut at a distance $z_{cut} = 9$ Å from the wall. An analogous integration can be performed over the volume surrounding an infinitely long pore with radius R_p yielding a semianalytical solution (see the work of Peterson et al.[23] or Appendix A in the work of Allen et al.[10]) given by

$$V_p(r) = \pi\tau\epsilon' \left[\frac{7\sigma'^{12}}{32} K_9(r) - \sigma'^6 K_3(r) \right], \qquad (A3)$$

where K_m is defined as the integral

$$K_m(r) = R_p^{-m} \int_0^\pi d\theta [-\eta\cos\theta + (1 - \eta^2\sin^2\theta)^{1/2}]^{-m} \qquad (A4)$$

with $\eta = r/R_p$ and r is the distance from the particle to the inner surface of the pore. In our simulations the corresponding forces are evaluated by numerical integration for the appropriate pore radius R_p, tabulated for 10 000 values and stored in each simulation run. For particle positions outside the pore ($z > 0$) of length L_p but radial distances $r < R_p$ we use a simple interpolation between the particle wall (A2) and particle pore (A3) potentials to avoid discontinuities

$$V_{wp}(r,z) = \frac{z}{\sqrt{z^2 + r^2}} V_w(z) + \frac{r}{\sqrt{z^2 + r^2}} V_p(r). \qquad (A5)$$

The interaction between the ions and the membrane surface is obtained in an analog way. The interaction parameters are summarized in Table I. Very similar interactions have been used by Allen et al. in their study of intermittency of water in a narrow hydrophobic pore.[10] We finally note that a consistent integration over a finite cylinder in a slab would yield a different, but very similar interaction to (A2)–(A5), which we think would affect our results only slightly in a quantitative way, but not qualitatively.

APPENDIX B: MEASUREMENT OF THE ELECTRIC FIELD

In order to evaluate the local electric field at a given position **r**, the electrostatic force per charge of all charged water atoms (oxygen, hydrogen) in a small volume around **r** is averaged over 10^3–10^4 independent configurations. The volume is cubic and centered on **r** with side lengths of 1 Å. Only the reciprocal part of the smooth particle-mesh Ewald force is taken into account to avoid delta peak contributions due to close proximity of surrounding charges.[16] These local contributions do not contribute to the macroscopic electric field at **r** and average out to zero. The Ewald cut-off radius was chosen to be $r_c = 2$ Å and the convergence parameter α was accordingly readjusted to $\alpha = 3.2/r_c$. This method yields the same result as obtained by integration of charge density along the z axis [one-dimensional (1D) Poisson equation], if the system is homogeneous in the x-y plane. Fixed phantom test particles, not acting on the other particles in the system, were used to measure the electric field in the case when no water molecules were present around **r** (e.g., in a pore empty of water).

APPENDIX C: ELECTRIC FIELD INSIDE THE PORE

Consider a schematic model whereby the cylindrical pore of radius R and length L and embedding dielectric medium of permittivity ϵ_m are confined between the two infinite plates of a condenser carrying uniform surface-charge densities $\pm r$. The water-filled pore is characterized by a permittivity ϵ_p, and the axis of the cylinder is chosen to be the z axis.
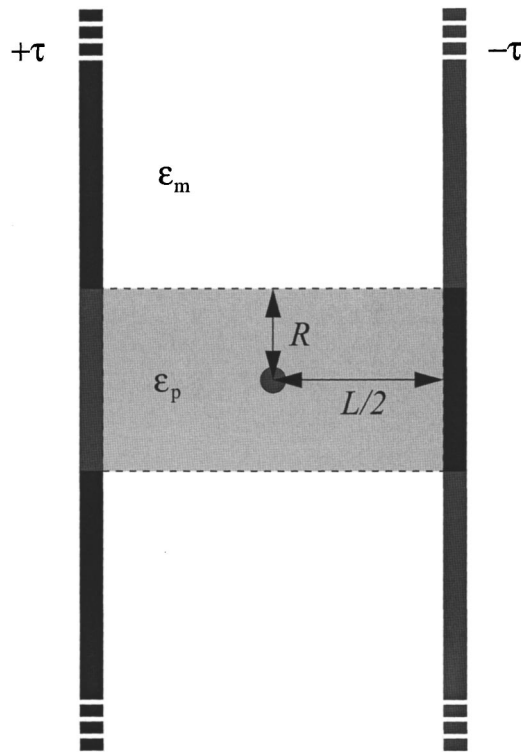
FIG. 15. Sketch of two infinite oppositely charged plates with charge density $\pm\tau$ separated by a distance L enclosing a medium with permittivity ϵ_m. The dielectric pore with permittivity ϵ_p between the plates generates surface charges which change the homogeneous field generated by these plates. The resulting field on the axis of the pore is given by Eq. (C1).

In the following, z is the distance from the left cylinder entrance. The setup is sketched in Fig. 15. In the absence of a cylindrical pore through the membrane, i.e., in the limit $R \to 0$, the electric field inside the condenser would be $\mathbf{E} = \tau/(\epsilon_o\epsilon_m)\mathbf{u}_z = E\mathbf{u}_z$. ($\mathbf{u}_z$ being the unit vector along Oz.) In the presence of the pore ($R > 0$), there will be a component of $\mathbf{E}$ normal to $\mathbf{u}_z$, which will be discontinuous at the pore/membrane interface. The longitudinal component is continuous, but will be affected by the presence of the dielectric continuum ϵ_p inside the pore.

Neglecting this effect, we invoke the superposition principle to calculate the axial component $E(z, r=0)$ along the cylinder axis ($r=0$) as the sum of the field due to the infinite plates in the absence of the pore, minus the field resulting from the two disks at the end of the pore (at 0 and L), plus the field due to these two disks when the pore contains a dielectric medium ϵ_p, i.e.,

$$
E(z, r=0) = \left\{ \frac{\tau}{\epsilon_0\epsilon_m} + \frac{\tau}{2\epsilon_0}\left[2 - \frac{z}{\sqrt{z^2+R^2}} \right. \right.
$$
$$
\left. \left. - \frac{L-z}{\sqrt{(L-z)^2+R^2}} \right]\left(\frac{1}{\epsilon_p} - \frac{1}{\epsilon_m}\right) \right\},
$$
$$
= \left\{ \frac{\tau}{\epsilon_0\epsilon_p} + \frac{\tau}{2\epsilon_0}\left[\frac{z}{\sqrt{z^2+R^2}} \right. \right.
$$
$$
\left. \left. - \frac{L-z}{\sqrt{(L-z)^2+R^2}} \right]\left(\frac{1}{\epsilon_p} - \frac{1}{\epsilon_m}\right) \right\}. \tag{C1}
$$

At the center of the pore ($z=L/2$), this reduces to

$$
E(z=L/2,\ r=0) = \frac{\tau}{\epsilon_0}\left[\frac{1}{\epsilon_p} + \frac{L}{\sqrt{L^2+4R^2}}\left(\frac{1}{\epsilon_m} - \frac{1}{\epsilon_p}\right) \right]. \tag{C2}
$$

At both ends

$$
E(z=0,\ r=0) = E(z=L,\ r=0)
$$
$$
= \frac{\tau}{\epsilon_0}\left[\frac{1}{\epsilon_p} + \frac{L/2}{\sqrt{L^2+R^2}}\left(\frac{1}{\epsilon_m} - \frac{1}{\epsilon_p}\right) \right]
$$
$$
< E(z=L/2,\ r=0) \quad \text{if } \epsilon_m < \epsilon_p. \tag{C3}
$$

The effective permittivity in the pore may then be estimated from

$$
\langle E \rangle \simeq E(z=L/2,\ r=0) = \frac{E_0}{\epsilon} = \frac{\tau}{\epsilon_0\epsilon}, \tag{C4}
$$

which yields

$$
\frac{1}{\epsilon} = \frac{1}{\epsilon_p} + \frac{L}{\sqrt{L^2+4R^2}}\left(\frac{1}{\epsilon_m} - \frac{1}{\epsilon_p}\right). \tag{C5}
$$

In fact, $\langle E \rangle < E(z=L/2, r=0)$, so that ϵ should be larger than predicted by Eq. (C5). The prediction (C5) of the macroscopic model is in semiquantitative agreement with the simulation data presented in Table II for pores of various radii (which corresponds to $\epsilon_p \gg \epsilon_m = 1$ leading to $\epsilon \simeq \sqrt{L^2+4R^2}/L$). Using the same macroscopic electrostatic model, we have calculated numerically the inhomogeneous electric-field distribution $E(r, z=z_c)$ off axis at the center of the pore. Results are shown in Fig. 4 and should be compared to the simulation data in Fig. 5. The comparison is commented in Sec. III B.

[1] See Special Issue, Water in confined geometries, edited by M. Rovere [J. Phys.: Condens. Matter **16**, S5297 (2004)].

[2] M. Watanabe, A. M. Brodsky, and W. Reinhardt, J. Phys. Chem. **95**, 4593 (1991).

[3] M. F. Toney, Nature (London) **368**, 444 (1994).

[4] B. Hille, *Ionic Channels of Excitable Membranes* (Sinauer, Sunderland, MA, 1992).

[5] G. Hummer, J. C. Rasaiah, and J. P. Nowortya, Nature (London) **414**, 188 (2001).

[6] O. Beckstein, P. C. Biggin, and M. S. P. Sansom, J. Phys. Chem. B **105**, 12902 (2001).

[7] O. Beckstein and M. S. P. Sansom, Proc. Natl. Acad. Sci. U.S.A. **100**, 7063 (2003).

[8] O. Beckstein and M. S. P. Sansom, Phys. Biol. **1**, 42 (2004).

[9] A. Anishkin and S. Sukharev, Biophys. J. **86**, 2883 (2004).

[10] R. J. Allen, S. Melchionna, and J.-P. Hansen, Phys. Rev. Lett. **89**, 175502 (2002); R. J. Allen, J.-P. Hansen, and S. Melchionna, J. Chem. Phys. **119**, 3905 (2003).

[11] S. M. Saparov and P. Pohl, Proc. Natl. Acad. Sci. U.S.A. **101**, 4805 (2004).

[12] M. E. Green and J. Lu, J. Phys. Chem. **101**, 6512 (1997).

[13] D. P. Chen and R. S. Eisenberg, Biophys. J. **64**, 1405 (1993).

[14] J. Piasecki, R. J. Allen, and J.-P. Hansen, Phys. Rev. E **70**, 021105 (2004).

[15] S.-H. Chung, T. W. Allen, and S. Kuyucak, Biophys. J. **83**, 263 (2002).

[16] P. S. Crozier, R. L. Rowley, N. B. Holladay, D. Henderson, and D. D. Busath, Phys. Rev. Lett. **86**, 2467 (2001).

[17] J. Dzubiella, R. J. Allen, and J.-P. Hansen, J. Chem. Phys. **120**, 5001 (2004).

[18] H. J. C. Berendsen, J. R. Grigera, and T. P. Straatsma, J. Phys. Chem. **91**, 6269 (1987).

[19] E. Spohr, Electrochim. Acta **44**, 1697 (1999).

[20] S. H. Lee and J. C. Rasaiah, J. Phys. Chem. **100**, 1420 (1996).

[21] R. Lynden-Bell and J. C. Rasaiah, J. Chem. Phys. **107**, 1981 (1997).

[22] C. Y. Lee, J. A. McCammon, and P. J. Rossky, J. Chem. Phys. **80**, 4448 (1984).

[23] B. K. Peterson, J. P. R. B. Walton, and K. E. Gubbins, J. Chem. Soc., Faraday Trans. 2 **82**, 1789 (1986).

[24] W. Smith and T. R. Forester, the DLPOLY_2 User Manual, 1999.

[25] D. Frenkel and B. Smit, *Understanding Molecular Simulation: From Algorithms to Applications* (Academic, San Diego, CA, 1996).

[26] U. Essmann, L. Perera, M. L. Berkowitz, T. Darden, H. Lee, and L. G. Pedersen, J. Chem. Phys. **103**, 8577 (1995).

[27] H. J. C. Berendsen, J. P. M. Postma, W. F. van Gunsteren, A. DiNola, and J. R. Haak, J. Chem. Phys. **81**, 3684 (1984).

[28] G. M. Whitesides and P. E. Laibinis, Langmuir **6**, 87 (1990).

[29] V. Ballenegger and J.-P. Hansen, Europhys. Lett. **63**, 381 (2003).

[30] Ph. Wernet *et al.*, Science **304**, 995 (2004).

[31] R. Lynden-Bell and J. C. Rasaiah, J. Chem. Phys. **105**, 9266 (1995).